

Phase-resolved optical frequency domain imaging

B. J. Vakoc, S. H. Yun, J. F. de Boer, G. J. Tearney, B. E. Bouma

Harvard Medical School and Wellman Center for Photomedicine,
Massachusetts General Hospital
50 Blossom Street, BAR-712, Boston, Massachusetts 02114
bvakoc@partners.org

Abstract: Phase-resolved Doppler optical coherence tomography has been used to image blood flow dynamics in various tissues using both time-domain and spectral-domain optical coherence tomography techniques. In this manuscript, we present phase-resolved Doppler imaging with a high-speed optical frequency domain imaging system. We demonstrate that by correcting for spurious timing-induced phase errors, excellent flow sensitivity can be achieved, limited only by the imaging signal-to-noise ratio. Conventional and Doppler images showing flow in an Intralipid phantom and in human skin are presented. Additionally, we demonstrate the ability of phase-resolved OFDI to measure high flow rates without the deleterious effects of fringe washout.

©2005 Optical Society of America

OCIS codes: (110.4500) Optical coherence tomography; (140.3600) Lasers, tunable; (170.3340) Laser Doppler velocimetry; (170.3880) Medical and biological imaging; (170.4500) Optical coherence tomography

References and Links

1. D. Huang, E. A. Swanson, C. P. Lin, J. S. Schuman, W. G. Stinson, W. Chang, M. R. Hee, T. Flotte, K. Gregory, C. A. Puliafito and J. G. Fujimoto, "Optical coherence tomography," *Science* **254** 1178 (1991)
2. Z. P. Chen, T. E. Milner, D. Dave and J. S. Nelson, "Optical Doppler tomographic imaging of fluid flow velocity in highly scattering media," *Opt. Lett.* **22** 64-66 (1997)
3. J. A. Izatt, M. D. Kulkarni, S. Yazdanfar, J. K. Barton and A. J. Welch, "In vivo bidirectional color Doppler flow imaging of picoliter blood volumes using optical coherence tomography," *Opt. Lett.* **22** 1439-1441 (1997)
4. J. K. Barton, J. A. Izatt, M. D. Kulkarni, S. Yazdanfar and A. J. Welch, "Three-dimensional reconstruction of blood vessels from in vivo color Doppler optical coherence tomography images," *Dermatology* **198** 355-361 (1999)
5. Z. P. Chen, T. E. Milner, S. Srinivas, X. J. Wang, A. Malekafzali, M. J. C. vanGemert and J. S. Nelson, "Noninvasive imaging of in vivo blood flow velocity using optical Doppler tomography," *Opt. Lett.* **22** 1119-1121 (1997)
6. M. C. Pierce, B. H. Park, B. Cense and J. F. de Boer, "Simultaneous intensity, birefringence, and flow measurements with high-speed fiber-based optical coherence tomography," *Opt. Lett.* **27** 1534-1536 (2002)
7. Y. Zhao, Z. Chen, C. Saxer, S. Xiang, J. F. de Boer and J. S. Nelson, "Phase-resolved optical coherence tomography and optical Doppler tomography for imaging blood flow in human skin with fast scanning speed and high velocity sensitivity," *Opt. Lett.* **25** 114 (2000)
8. B. R. White, M. C. Pierce, N. Nassif, B. Cense, B. H. Park, G. J. Tearney, B. E. Bouma, T. C. Chen and J. F. de Boer, "In vivo dynamic human retinal blood flow imaging using ultra-high-speed spectral domain optical Doppler tomography," *Opt. Express* **11** (2003)
<http://www.opticsexpress.org/abstract.cfm?URI=OPEX-11-25-3490>
9. S. Yazdanfar, A. M. Rollins and J. A. Izatt, "Imaging and velocimetry of the human retinal circulation with color Doppler optical coherence tomography," *Opt. Lett.* **25** 1448 (2000)
10. V. X. D. Yang, M. L. Gordon, T. Shou-jiang, N. E. Marcon, G. Gardiner, Q. Bing, S. Bisland, E. Seng-Yue, S. Lo, J. Pekar, B. C. Wilson and I. A. Vitkin, "High speed, wide velocity dynamic range Doppler optical coherence tomography (Part III): in vivo endoscopic imaging of blood flow in the rat and human gastrointestinal tracts," *Opt. Express* **11** (2003)
<http://www.opticsexpress.org/abstract.cfm?URI=OPEX-11-19-2416>
11. A. F. Fercher, C. K. Hitzenberger, G. Kamp and S. Y. Elzaiat, "Measurement Of Intraocular Distances By Backscattering Spectral Interferometry," *Opt. Commun.* **117** 43-48 (1995)
12. G. Hausler and M. W. Lindner, "Coherence radar and spectral radar - new tools for dermatological diagnosis," *J. Biomed. Opt.* **3** 21-31 (1998)

13. M. A. Choma, M. V. Sarunic, C. H. Yang and J. A. Izatt, "Sensitivity advantage of swept source and Fourier domain optical coherence tomography," *Opt. Express* **11** 2183-2189 (2003)
<http://www.opticsexpress.org/abstract.cfm?URI=OPEX-11-18-2183>
14. J. F. de Boer, B. Cense, B. H. Park, M. C. Pierce, G. J. Tearney and B. E. Bouma, "Improved signal-to-noise ratio in spectral-domain compared with time-domain optical coherence tomography," *Opt. Lett.* **28** 2067-2069 (2003)
15. R. Leitgeb, C. K. Hitzenberger and A. F. Fercher, "Performance of fourier domain vs. time domain optical coherence tomography," *Opt. Express* **11** 889-894 (2003)
<http://www.opticsexpress.org/abstract.cfm?URI=OPEX-11-8-889>
16. S. H. Yun, G. J. Tearney, B. E. Bouma, B. H. Park and J. F. de Boer, "High-speed spectral-domain optical coherence tomography at 1.3 μm wavelength," *Opt. Express* **11** 3598-3604 (2003)
<http://www.opticsexpress.org/abstract.cfm?URI=OPEX-11-26-3598>
17. S. H. Yun, G. J. Tearney, J. F. de Boer, N. Ifimia and B. E. Bouma, "High-speed optical frequency-domain imaging," *Opt. Express* **11** 2953-2963 (2003)
<http://www.opticsexpress.org/abstract.cfm?URI=OPEX-11-22-2953>
18. N. Nassif, B. Cense, B. H. Park, S. H. Yun, T. C. Chen, B. E. Bouma, G. J. Tearney and J. F. de Boer, "In vivo human retinal imaging by ultrahigh-speed spectral domain optical coherence tomography," *Opt. Lett.* **29** 480-482 (2004)
19. M. Wojtkowski, T. Bajraszewski, P. Targowski and A. Kowalczyk, "Real-time in vivo imaging by high-speed spectral optical coherence tomography," *Opt. Lett.* **28** 1745-1747 (2003)
20. M. V. Sarunic, M. A. Choma, C. H. Yang and J. A. Izatt, "Instantaneous complex conjugate resolved spectral domain and swept-source OCT using 3x3 fiber couplers," *Opt. Express* **13** 957-967 (2005)
<http://www.opticsexpress.org/abstract.cfm?URI=OPEX-13-3-957>
21. R. Huber, M. Wojtkowski, K. Taira, J. G. Fujimoto and K. Hsu, "Amplified, frequency swept lasers for frequency domain reflectometry and OCT imaging: design and scaling principles," *Opt. Express* **13** 3513-3528 (2005)
<http://www.opticsexpress.org/abstract.cfm?URI=OPEX-13-9-3513>
22. J. Zhang, J. S. Nelson and Z. P. Chen, "Removal of a mirror image and enhancement of the signal-to-noise ratio in Fourier-domain optical coherence tomography using an electro-optic phase modulator," *Opt. Lett.* **30** 147-149 (2005)
23. R. A. Leitgeb, L. Schmetterer, W. Drexler, A. F. Fercher, R. J. Zawadzki and T. Bajraszewski, "Real-time assessment of retinal blood flow with ultrafast acquisition by color Doppler Fourier domain optical coherence tomography," *Opt. Express* **11** 3116-3121 (2003)
<http://www.opticsexpress.org/abstract.cfm?URI=OPEX-11-23-3116>
24. S. H. Yun, G. J. Tearney, J. F. de Boer and B. E. Bouma, "Motion artifacts in optical coherence tomography with frequency-domain ranging," *Opt. Express* **12** 2977-2998 (2004)
<http://www.opticsexpress.org/abstract.cfm?URI=OPEX-12-13-2977>
25. W. Y. Oh, S. H. Yun, G. J. Tearney and B. E. Bouma, "115 kHz tuning repetition rate ultrahigh-speed wavelength-swept semiconductor laser," Submitted to *Optics Letters* (2005)
26. W. Y. Oh, S. H. Yun, G. J. Tearney and B. E. Bouma, "Wide tuning range wavelength-swept laser with two semiconductor optical amplifiers," *IEEE Photonics Tech. L.* **17** 678-680 (2005)
27. B. E. Bouma, G. J. Tearney, C. C. Compton and N. S. Nishioka, "High-resolution imaging of the human esophagus and stomach in vivo using optical coherence tomography," *Gastrointest. Endosc.* **51** 467-474 (2000)
28. I. K. Jang, B. E. Bouma, D. H. Kang, S. J. Park, S. W. Park, K. B. Seung, K. B. Choi, M. Shishkov, K. Schlendorf, E. Pomerantsev, S. L. Houser, H. T. Aretz and G. J. Tearney, "Visualization of coronary atherosclerotic plaques in patients using optical coherence tomography: Comparison with intravascular ultrasound," *J. Am. Coll. Cardiol.* **39** 604-609 (2002)
29. B. H. Park, M. C. Pierce, B. Cense, S. H. Yun, M. Mujat, G. J. Tearney, B. E. Bouma and J. F. de Boer, "Real-time fiber-based multi-functional spectral-domain optical coherence tomography at 1.3 μm ," *Opt. Express* **13** 3931-3944 (2005)
<http://www.opticsexpress.org/abstract.cfm?URI=OPEX-13-11-3931>
30. S. Yazdanfar, C. H. Yang, M. V. Sarunic and J. A. Izatt, "Frequency estimation precision in Doppler optical coherence tomography using the Cramer-Rao lower bound," *Opt. Express* **13** 410-416 (2005)
<http://www.opticsexpress.org/abstract.cfm?URI=OPEX-13-2-410>
31. S. H. Yun, C. Boudoux, G. J. Tearney and B. E. Bouma, "High-speed wavelength-swept semiconductor laser with a polygon-scanner-based wavelength filter," *Opt. Lett.* **28** 1981-1983 (2003)

1. Introduction

Optical coherence tomography (OCT) provides cross-sectional images of biological samples with resolution on the scale of several to tens of microns [1]. Microstructural contrast in conventional OCT results from differences in the optical scattering properties of various tissues. Additional biological or functional information can be obtained through the

application of Doppler techniques to measure spatially-localized motion in the sample [2, 3]. These methods, termed color Doppler OCT or optical Doppler tomography, have been applied for imaging blood flow in the skin [3-7], retina [8, 9], and esophagus [10], among others. Simultaneous imaging of tissue microstructure and blood flow can significantly enhance the diagnostic utility of OCT. Initial Doppler OCT measurements were performed with time-domain OCT (TD-OCT) systems. Recently, it has been demonstrated that the application of frequency-domain ranging techniques [11, 12] to OCT results in significantly improved sensitivity [13-15] and imaging speed [16, 17] compared with conventional TD-OCT. Frequency-domain ranging has been implemented in OCT in two configurations, spectral-domain OCT (SD-OCT) [16, 18, 19] and optical frequency domain imaging (OFDI) [17, 20-22]. In SD-OCT, a spectrometer is used to record spectral fringes that result from the interference of a reference beam with light reflected from a sample. In OFDI, a narrowband wavelength-swept source and a single detector are used to record the same interferogram. Doppler imaging has been demonstrated recently in SD-OCT systems [8, 23] but not, to our knowledge, in high-speed OFDI systems. Since OFDI is less prone to motion-induced fringe washout effects [24] associated with endoscopy and can provide a significantly larger depth range, it may become a preferred method for certain biomedical applications. Continued development of wavelength-swept laser sources promises further improvements in imaging speed [25] and resolution [26]. These advantages are compelling in several OCT applications, including Barrett's esophagus screening [27] and coronary imaging [28]. Combining OFDI with functional contrast through flow imaging may lead to an improved diagnostic capability, especially in screening for early cancer. In this manuscript, we demonstrate a high-speed phase-resolved OFDI system suitable for high-sensitivity flow measurements. A method for removing timing-induced noise that would otherwise limit flow sensitivity is presented, and the resulting system is shown to have signal-to-noise ratio (SNR) limited phase sensitivity. The capabilities of the phase-resolved OFDI system are demonstrated by imaging an Intralipid flow phantom and human dermal vessels *in vivo*.

2. Principle of Phase Resolved OCT

Phase-resolved OCT systems measure both the amplitude and phase of the light reflected from the sample as a function of depth. The amplitudes are used to generate traditional OCT structural images. Although the phases are generally random for biological samples, additional functional information can be obtained by measuring changes in phase. For example, spatially-resolved flow imaging can be accomplished by comparing the phases between successive A-lines at the same depth. A translation of the sample by distance δ during the time interval between two A-lines will induce a change in the measured phase of the reflected light given by $\Delta\phi = 2n\langle k \rangle\delta$, where n is the refractive index of the sample and $\langle k \rangle$ is the average wavenumber of the OCT source ($k=2\pi/\lambda$). Calculating this phase difference at each depth yields spatially-resolved measurements of both the magnitude and direction of the axial (parallel to the imaging beam) flow velocity. Assuming that the imaging beam intersects the flow velocity vector at an angle β , the flow velocity is given by $v = \Delta\phi(2n\langle k \rangle\tau \cos(\beta))^{-1}$ where τ is the time between A-lines. This method was originally demonstrated in TD-OCT [7] and later in SD-OCT [8], and is the method applied in the current work. To ensure correlation between the phase measurements of successive A-lines, the transverse displacement of the imaging beam between A-lines must be small relative to the beam size. This constraint can be met by effectively over sampling in the transverse direction.

The sensitivity of the flow measurement is fundamentally limited by the phase sensitivity of the OCT system, which, in turn, is limited by the OCT system noise floor. It has been shown that the noise in the measured phase difference of a given signal, $\sigma_{\Delta\phi}^2$ (rad²), with an SNR given by X can be written as [29, 30],

$$\sigma_{\Delta\phi}^2 = \left(\frac{1}{X} \right). \quad (1)$$

Note that, because calculation of the phase difference requires two measurements of phase, the noise level of phase difference measurements as given by Eq. (1) is twice that of single phase measurements. Most signals reflected from biological samples have SNRs below 50 dB, suggesting an ultimate phase difference measurement accuracy of ~ 3 mrad (this corresponds to a flow velocity of 0.02 mm/s at $\beta = 80^\circ$, $n = 1.3$, and $\tau^{-1} = 15.6$ kHz). Signals returning from depths greater than several hundred microns, where blood vessels are likely to be located, typically have SNRs below 30 dB and would yield ultimate phase accuracies of ~ 30 mrad. To achieve high-sensitivity flow imaging, other (less fundamental) noise sources, including interferometric instabilities, should be minimized such that phase sensitivity is SNR-limited up to an SNR of approximately 50 dB.

3. Phase-Resolved OFDI

Because flow is calculated from the phase difference between successive A-lines, it is essential that phase measurements be repeatable from one A-line to the next. Changes in the measured phase resulting from systematic or interferometric instabilities increase the phase noise floor of the system, reducing the ability of the system to image low flow rates. In SD-OCT, the inherent stability of the source, interferometer, and spectrometer enables highly repeatable phase measurements and, correspondingly, high-sensitivity flow imaging. In OFDI, variations in the synchronization/timing of the wavelength-swept source relative to the acquisition electronics can induce variations in the measurement of phase that degrade sensitivity. This effect is examined in the following section.

3.1 Impact of source/acquisition timing variations in phase-resolved OFDI

Figure 1 depicts the OFDI system used in this paper [17]. The system comprises three modules: the wavelength-swept source, the interferometer, and the digital acquisition (DAQ) electronics. The source is constructed from a fiber ring-laser using a semiconductor optical amplifier (SOA) as the gain element. An intracavity rapidly-tuned narrowband optical filter is constructed using a polygon mirror [31]. Each facet of the polygon mirror generates a single sweep of the laser output as it rotates through the beam path of the telescope. The source has an output wavelength range from 1278 nm to 1388 nm, a repetition rate of 15.6 kHz, and an instantaneous linewidth of ~ 0.13 nm. The polarized source output is coupled to the interferometer where it is split into a reference arm and a sample arm. The sample arm light is delivered to and collected from the sample through a single fiber. An optical circulator directs the reflected light to the interferometer output coupler. The reference arm light reflects from the reference mirror, passes through a polarizer to remove any acquired variation in polarization state as a function of wavelength, and is directed to the other port of the output coupler. Resulting interference fringes are detected on both output ports. These signals are subtracted in a balanced-receiver configuration that reduces source intensity noise as well as auto-correlation noise from the sample. A portion of the reference arm light is directed to a narrowband fiber Bragg grating (FBG). A reflected optical pulse is generated when the wavelength of the source matches the FBG reflection wavelength. This pulse is detected and converted into a TTL signal with a low-to-high transition that is coincident with the optical pulse and a high-to-low transition that is electrically tunable.

The DAQ board (National Instruments NI-6115, 10 MS/s) digitizes the balanced-receiver output using the high-to-low transition of the FBG-generated TTL pulse as a trigger signal. In response to the trigger signal, the DAQ board performs N analog-to-digital (A2D) conversions at its internal sample clock rate where the conversion occurs on the sample clock transitions. Although the polygon filter is driven by a signal derived from the sample clock, the phasing of the swept source output and the sample clock drifts slowly over time, causing the trigger signal to fall arbitrarily within the sample clock cycle. As a result, the delay between the trigger signal and the subsequent A2D conversion can vary by one period of the sample clock.

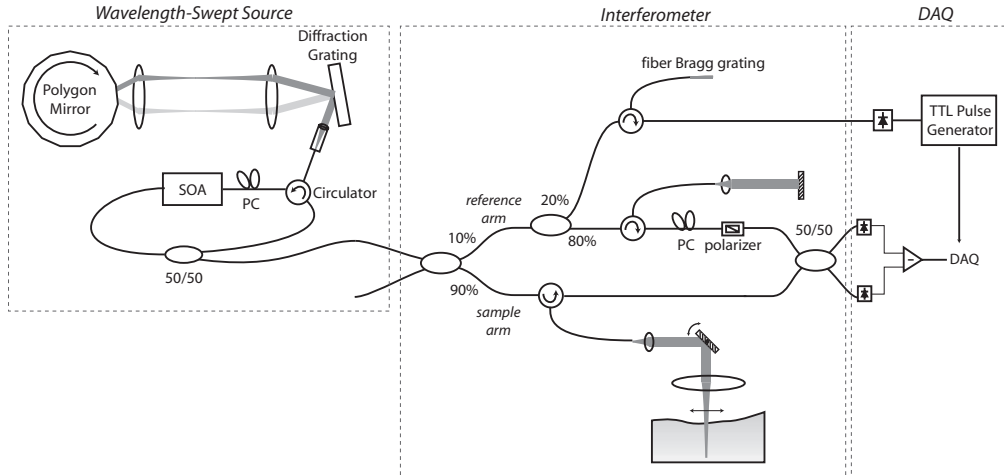


Fig. 1. Basic configuration of the OFDI system.

To understand how this variation in delay affects phase-resolved measurements, consider the interference fringe resulting from a stationary mirror at depth z with reflectivity R . The resulting interference signal, $S(t)$, is given by

$$S(t) \propto \sqrt{R} \cos(2k_o z + 2\alpha z[t + \varepsilon]) \quad (2)$$

where the laser is assumed to sweep linearly in wavenumber, i.e., $k(t) = k_o + \alpha t$ ($\alpha = -6.1 \times 10^9 \text{ m}^{-1}\text{s}^{-1}$ for our source). Because in practice the source sweep contains higher-order terms, the detected signal is resampled in time to recover a signal given by Eq. (2) [17]. The parameter ε describes the delay between the trigger signal and the subsequent A2D conversion. This delay ranges from 0 to the sample clock period T_{cl} ($= 0.1 \mu\text{s}$) and is different for each A-line. The phase of the interference fringe associated with the mirror is given by $\phi = 2k_o z + 2\alpha z\varepsilon$, and the range of phase differences between successive A-lines, $\Delta\phi$, is given by

$$|\Delta\phi| = 2\alpha z |\Delta\varepsilon| \leq 2\alpha z T_{cl} \equiv \pi Z. \quad (3)$$

where $\Delta\varepsilon$ is the change in the delay, ε , from one A-line to the next and is maximally equal to T_{cl} . A normalized depth parameter $Z = 2z\alpha T_{cl}/\pi$ has been defined where $Z = 0$ at the path-matched depth and $Z = 1$ at the Nyquist-limited imaging depth. Equation 3 indicates that timing variations produce phase jumps that increase linearly with depth up to maximum value of π at the Nyquist-limited imaging depth ($Z = 1$). As shown previously, SNR-limited noise levels can be as low as a several mrad and therefore phase differences of the magnitude predicted by Eq. (3), if uncorrected, would severely degrade the sensitivity of the system.

3.2 Correction of timing-induced errors

There are several potential methods to correct the timing-induced phase jumps. Optical generation of the sample clock would improve the synchronization between the source and the DAQ board and reduced timing-induced phase jumps. To achieve this, a small portion of the source output could be directed to a periodic optical filter, generating an optical clock signal that is converted to a suitable TTL sample clock signal [20]. When the laser sweeps nonlinearly in k , the resulting sample clock is frequency chirped, and abruptly changes frequency between the end of one sweep and the beginning of the next. As such, there are potential compatibility issues between optically generated clocks and higher-speed ($\sim 100 \text{ MS/s}$) DAQ boards which incorporate phase-locked loop circuits on the external sample clock input. A second solution is to subtract from the measured phase-difference of each A-line pair that portion which varies linearly with depth in a manner similar to a correction technique

applied in phase-resolved TD-OCT systems [6]. Although straightforward and likely valid for cases in which flow is localized in a small region, this approach can distort the measured flow by subtracting linear portions of actual flow distributions.

To allow for the accurate measurement of arbitrary flow distributions, we have implemented a solution in which a separate calibration signal is used to measure timing-induced phase variations. These variations are then subtracted from the measured phase differences at all remaining depths. Figure 2(a) shows a sample arm modified to provide this calibration signal. A 1% tap coupler is used to direct light to both a stationary calibration mirror (1% port) and the sample to be imaged (99% port). The calibration mirror is positioned such that its resultant signal appears near the maximum imaging depth, which is optimal for two reasons. Firstly, the calibration mirror creates a line artifact in the image. By locating the calibration mirror near the maximum imaging depth, this artifact appears near the image edge, minimizing the degree to which it can obscure the sample image. Secondly, the magnitude of the timing-induced phase differences is maximized at large depths and can therefore be most accurately measured at these depths. Hereafter, the signal from the calibration mirror is referred to as the calibration signal and the signal from the sample is referred to as the sample signal. The amplitude of the calibration signal is adjusted to ensure that it is large enough to dominate the sample signal at large depths but not so large that it induces significant auto-correlation noise [12]. Figure 2(b) shows a representative A-line from a tissue image. Notice that the calibration signal obscures only a small portion of the image near the edge of the imaging depth.

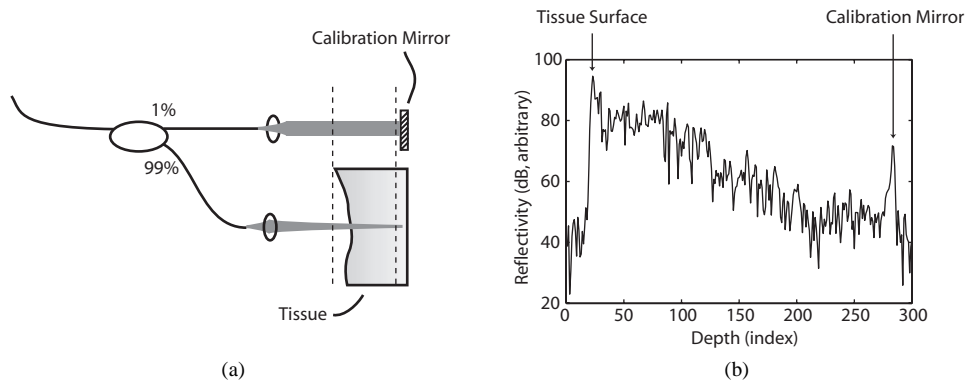


Fig. 2. (a) The implementation of a calibration mirror used to generate a calibration signal which allows measurement of the timing-induced phase variations for each A-line pair. (b) A representative A-line showing the signal from the sample (tissue) and the calibration signal.

Corrected phase differences are calculated by subtracting a fraction of the measured phase difference of the calibration signal from the measured phase difference of the sample signal. The magnitude of the applied correction is scaled linearly with the sample signal depth as dictated by Eq. (3). In the following, the parameters $\Delta\phi_{i,j}$ and $\hat{\Delta}\phi_{i,j}$ are used to describe the directly measured phase difference and calculated corrected phase difference, respectively, at depth index i between A-lines j and $(j-1)$. If the calibration signal is located at depth index m , the corrected phase difference at depth index i is calculated as

$$\hat{\Delta}\phi_{i,j} = \Delta\phi_{i,j} - \left(\frac{i}{m}\right)\Delta\phi_{m,j} . \quad (4)$$

The first term is the measured phase difference at depth index i and the second term is the applied correction, scaled according to the sample signal depth by the multiplicative factor (i/m) . Appropriate phase unwrapping is performed on all measurements. Finally, bulk motion artifacts can be removed by subtracting the median phase difference from each A-line pair [6].

3.3 Measured phase sensitivity

The phase sensitivity of the system is given by the noise level of the corrected phase differences. Ideally, the correction procedure described by Eq. (4) reduces the impact of timing-induced phase jumps to negligible levels, leaving only the fundamental SNR-limited noise. To test this, a stationary mirror was used to generate a sample signal and corrected phase differences were calculated according to Eq. (4). The measured phase (ϕ), phase difference ($\Delta\phi$), and corrected phase difference ($\hat{\Delta\phi}$) of a sample signal at depth $Z = 0.54$ are plotted in Fig. 3(a)-(c), respectively. A depth of $Z = 1$ corresponds to 2.6 mm in these measurements. The imperfect synchronization between the source and sample clock can be seen in the slow drift of the measured phase (Fig. 3(a)). The large jumps in phase occur when the acquisition delay switches by one clock cycle. The magnitude of these phase jumps (see scale bar on right of Fig. 3(b)) is in agreement with the prediction of Eq. (3) for a signal at this depth. Figure 3(c) shows that the large phase jumps have been eliminated in the corrected phase difference. Additionally, the baseline noise level has been reduced by 7 dB due to the correction of smaller phase jumps resulting from variations in acquisition delay that are less than one clock cycle.

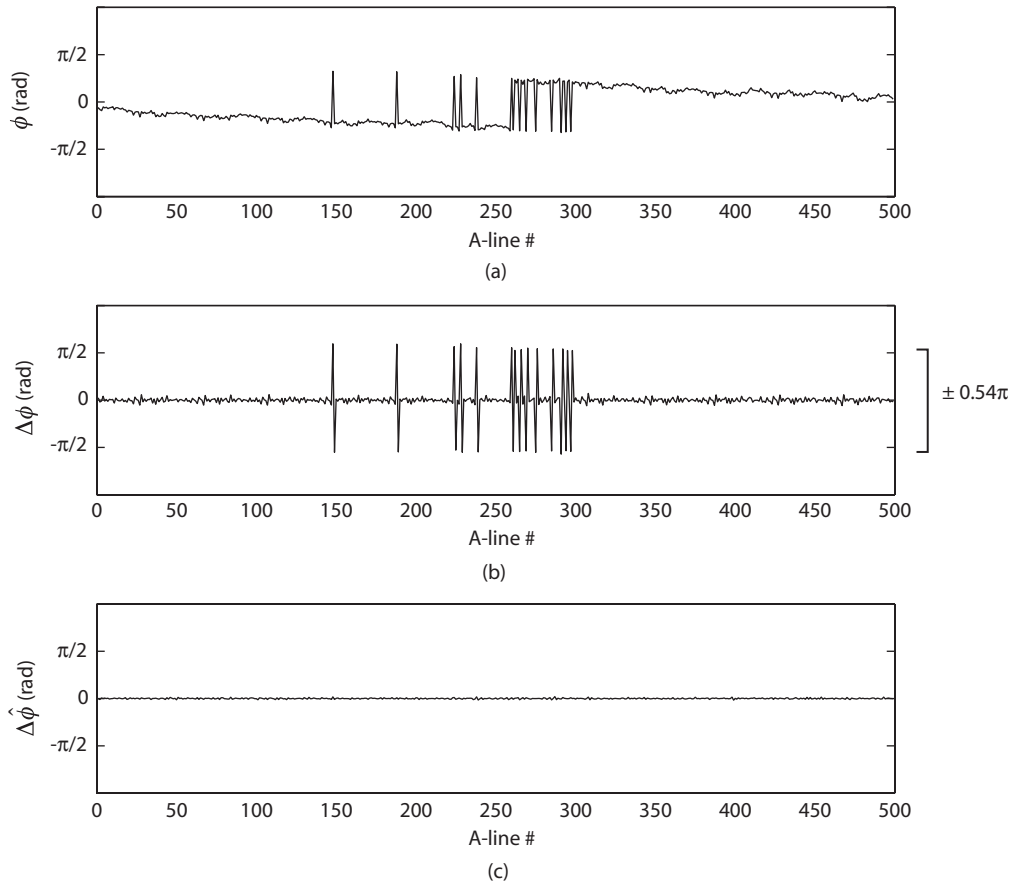


Fig. 3. A typical measured phase (a), phase difference (b), and corrected phase difference (c) for a sample signal at depth $Z = 0.54$.

To confirm the effectiveness of the correction method, the noise on the corrected phase differences was measured and compared to the SNR-limited noise predicted by Eqs. (1) and (4) as

$$\sigma_{\Delta\phi}^2 = \left(\frac{1}{X_s}\right) + \left(\frac{Z_s}{Z_c}\right)^2 \left(\frac{1}{X_c}\right) \quad (5)$$

where X_s is the SNR of the sample signal located at depth Z_s and X_c is the SNR of the calibration signal located at depth Z_c . Phase difference measurements were performed at sample signal depths of $Z_s = 0.07$ (0.2 mm), 0.54 (1.4 mm), and 0.84 (2.2 mm). In all measurements, the calibration signal was located at depth $Z_c = 0.96$ (2.50 mm) and had an SNR $X_c \sim 31$ dB. The sample signal SNR, X_s , at each depth was adjusted from 10 dB to 50 dB through the use of a variable neutral-density filter located in the sample arm. Figure 4 plots the measured noise (calculated from 500 measurements) as a function of the sample signal SNR for two of the measured depths. The measurements show excellent agreement with the predicted noise level given by Eq. (5). Measurements at the intermediate depth of $Z_s = 0.54$ (not shown) also show excellent agreement with predictions. This agreement indicates that the proposed correction method is able to reduce timing-induced phase noise to negligible levels for this range of SNRs.

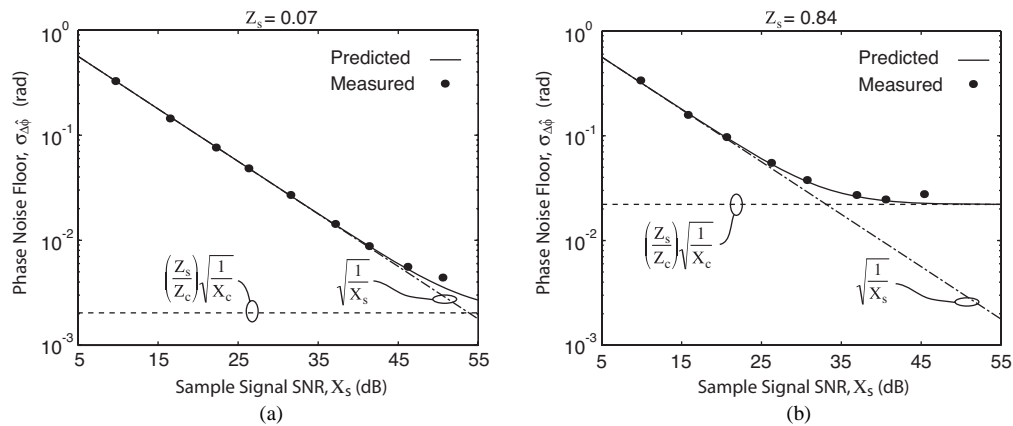


Fig. 4. The measured (circle) and predicted (solid curve) phase noise as a function of the sample signal SNR (X_s) at depths (a) $Z_s = 0.07$ and (b) $Z_s = 0.84$. The individual contribution to the overall noise resulting from only the sample signal noise (dash-dot curve) and calibration signal noise (dashed curve) are also shown. In both cases, the calibration signal was located at a depth $Z_c = 0.96$ with $X_c \sim 31$ dB.

As indicated by Eq. (5), both the noise in the sample signal (first term) and the noise in the calibration signal (second term) contribute to the noise in the corrected signal, with the calibration signal contribution scaling with the sample signal depth, Z_s . At the large depth shown in Fig 4(b), the calibration signal noise dominates when the sample signal SNR exceeds ~ 35 dB. Assuming that, in practice, the SNR of sample signals from large depths is limited below 30 dB, and that from shallow depths is limited below 50 dB, one can see from Fig. 4 that the resulting noise over this range is sample signal SNR-limited. In the event of higher sample signal SNRs, the calibration signal SNR can be increased to reduce its noise contribution.

3.4 Images

As a test of the phase-resolved OFDI system and correction method described above, pulsatile flow of 0.25% Intralipid in an 800 μm tube surrounded by stationary Intralipid of the same concentration was imaged. The angle between the tube and imaging beam was set at 80° . Figure 5 shows the resulting structural and flow images. The images were acquired at an A-line rate of 15.6 kHz and are 3 mm in width and 2.6 mm in depth (in air). Each frame contains

2000 A-lines (displacement of 1.5 μm per A-line) yielding a frame rate of 7.8 frames per second. A moving median filter of size (20 x 3) pixels (30 x 25 μm) was applied to the corrected phase (flow) image. The flow image clearly differentiates the region of flow inside the tube from the surrounding stationary Intralipid. The phase difference and corresponding flow velocity (assuming an index of refraction of $n = 1.32$) are given in the colorbar. As mentioned previously, OFDI does not suffer from fringe washout due to sample motion. As such, phase-resolved OFDI is well-suited to measure high flow rates that induce phase shifts greater than 2π . To demonstrate this, the imaging beam was positioned at the center of the tube shown in Fig. 5 and A-lines were recorded without scanning the beam while an increased pulsatile flow rate was induced. Figure 6(a) shows the resulting M-mode image. Phase is mapped to a color-scale and the image coordinates are depth index (vertical axis) and time (horizontal axis). The increased flow rate results in measured phase differences that exceed 2π and produce phase wrapping artifacts. Because OFDI does not suffer from fringe washout effects, no SNR penalty is incurred as a result of these large phase shifts. The apparent depth, however, is displaced from the actual depth due to the large Doppler shift [24], an artifact that does not directly impact the ability of OFDI to measure large flow rates. Figure 6(b) shows the phase image unwrapped to remove discontinuities of 2π , yielding the depth-resolved time-varying flow distribution in the tube. Note the change of color-scale between Fig. 6(a) and 6(b). Figure 6(c) shows an unwrapped flow profile acquired at the time T as marked in the phase images. The images shown in Figure 6 are constructed by averaging over 100 consecutive A-lines. Figure 7 shows cross-sectional structural and flow images obtained from a human nailbed *in vivo*. The image size is the same as in Fig. 5. Two blood vessels (circled), not observed in the structural image, can be clearly seen in Fig. 7(b).

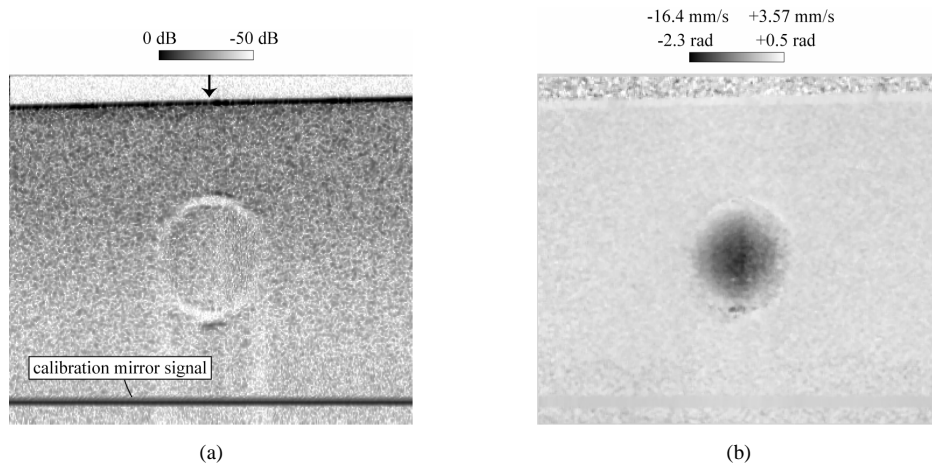


Fig. 5. Images of Intralipid flow through an 800 μm tube immersed in stationary Intralipid. (a) Structural image. (b) Flow image. The transverse distance is 3 mm and the imaging depth is 2.6 mm in air. Each image comprises 2000 A-lines.

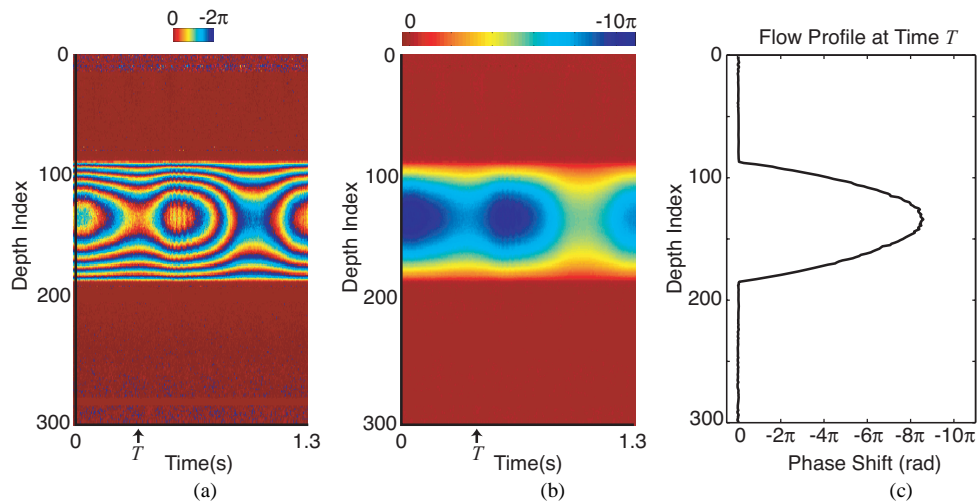


Fig. 6. M-mode image showing depth-resolved Intralipid flow as a function of time for high-rate, pulsatile flow. The beam was positioned at the center of the tube (see arrow in Fig. 5). In (a), the measured phase difference is shown without unwrapping phase discontinuities. In (b), a phase unwrapping algorithm is used to reconstruct the flow. Note the difference in scale between the images. In (c) the flow profile at time T (indicated on the time axis) is plotted. The maximum flow in (c) induced a phase difference of -8.5π corresponding to a flow rate of 191 mm/s.

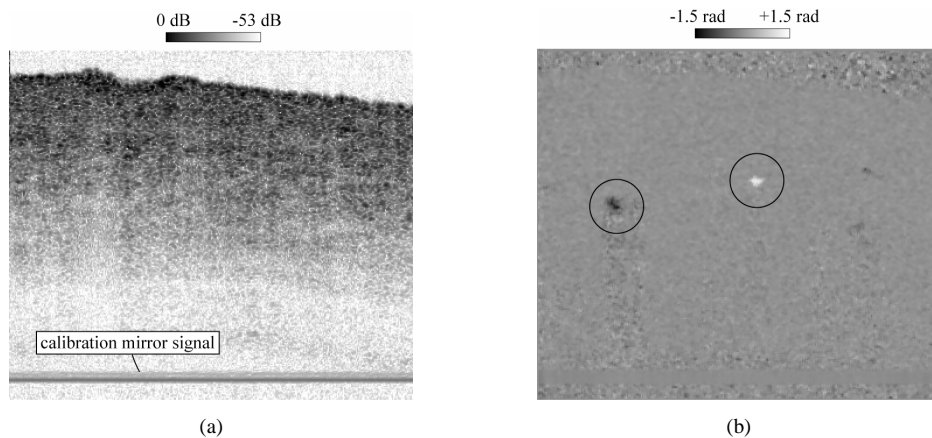


Fig. 7. Images of human finger near the nailbed. Fig. 7(a) shows the structural image and 7(b) shows the flow image. Two blood vessels (circled) are clearly visible in the flow image. The transverse dimension is 3 mm and the depth is 2.6 mm. Each image contains 2000 A-lines.

4. Conclusion

We have presented what we believe to be the first implementation of high-speed phase-resolved OFDI. The origin of timing-induced phase errors was explained and a method for removing them was demonstrated. The phase sensitivity was shown to be SNR-limited at several depths up to an SNR of 50 dB. Structural and flow images of a phantom of Intralipid flowing through a tube and blood flow in human skin, each acquired at an A-line rate of 15.6 kHz, were presented. The ability of phase-resolved OFDI to measure high flow rates in which phase differences significantly exceed 2π without fringe-washout effects was demonstrated.

Flow imaging through phase-resolved OFDI has the potential to enhance the diagnostic capabilities and the clinical impact of future OFDI-based systems.

Acknowledgments

This research was supported in part by the National Institutes of Health contracts R01 HL70039, R33 CA110130, R01 HL076398, R01 CA103769, and R01 RR0119768.